Correspondence and
requests for materials
should be addressed to
C.S.O. (cozkan@engr.
ucr.edu)

Hydrous Ruthenium Oxide Nanoparticles Anchored to Graphene and Carbon Nanotube Hybrid Foam for Supercapacitors

Wei Wang[1], Shirui Guo[3], Ilkeun Lee[4], Kazi Ahmed[2], Jiebin Zhong[1], Zachary Favors[1], Francisco Zaera[4], Mihrimah Ozkan[2] & Cengiz S. Ozkan[1]

[1]Materials Science and Engineering Program, Department of Mechanical Engineering, Department of Electrical Engineering, University of California, Riverside, CA 92521 (USA), [2]Department of Electrical Engineering, University of California, Riverside, CA 92521 (USA), [3]Lawrence Livermore National Lab, Physical and Life Sciences Directorate, Livermore, CA, 94550 (USA), [4]Department of Chemistry, University of California, Riverside, CA 92521 (USA).

In real life applications, supercapacitors (SCs) often can only be used as part of a hybrid system together with other high energy storage devices due to their relatively lower energy density in comparison to other types of energy storage devices such as batteries and fuel cells. Increasing the energy density of SCs will have a huge impact on the development of future energy storage devices by broadening the area of application for SCs. Here, we report a simple and scalable way of preparing a three-dimensional (3D) sub-5 nm hydrous ruthenium oxide (RuO_2) anchored graphene and CNT hybrid foam (RGM) architecture for high-performance supercapacitor electrodes. This RGM architecture demonstrates a novel graphene foam conformally covered with hybrid networks of RuO_2 nanoparticles and anchored CNTs. SCs based on RGM show superior gravimetric and per-area capacitive performance (specific capacitance: 502.78 F g^{-1}, areal capacitance: 1.11 F cm^{-2}) which leads to an exceptionally high energy density of 39.28 Wh kg^{-1} and power density of 128.01 kW kg^{-1}. The electrochemical stability, excellent capacitive performance, and the ease of preparation suggest this RGM system is promising for future energy storage applications.

Among all energy storage devices, supercapacitors (SC) have garnered substantial attention in recent years due to their ultra-fast charge and discharge rate, excellent stability, long cycle life, and very high power density. These characteristics are desirable for many applications including electric vehicles (EVs) and portable electronics[1,2]. However, SCs may only serve as standalone power sources in systems that require power delievery for a short duration (<10 sec). This is due to their relatively lower energy density in comparison to other types of energy storage devices such as batteries and fuel cells[1]. In often cases SCs are used as part of a hybrid system with other high energy storage devices in real applications. Therefore, boosting the energy density of SCs has become one of the most promising methods for the development of future high energy and high power density energy storage devices. Energy density (E) is equal to $0.5CV^2$, where C is the specific capacitance and V is the operational voltage window. A boost in energy density can be achieved by increasing one or both of the specific capacitance and voltage windows. Moreover, power density is defined as $P = V^2/4R$, where $R = \rho L/A$. Here, R is equivalent series resistance (ESR) of the SC and ρ, L, A are the specific electrical resistance, length of current flow, and area of current flow, respectively. Thus, high capacitance is critical to achieve higher energy density while large electrochemically accessible surface area, high electrical conductivity, short ion diffusion pathways, and excellent interfacial integrity are critical to achieve higher power density. Additionally, both power density and energy density can be increased by the widening of the operational voltage window. Nanostructured active materials provide a mean to these ends and are crucial in fabricating high-performance SCs[3–8].

There are two types of electrochemical capacitors: (i) electrochemical double layer capacitors (EDLCs), which are generally based on pure graphitic nanostructures including CNTs, graphene, carbon onions/spheres, template derived carbons, activated carbon, etc[4,9–14]. and (ii) pseudocapacitors which are based on pseodocapacitive materials like V_2O_5[15,16], RuO_2[17], MnO_2[18], Co_2O_3[19], Co_3O_4[20], In_2O_3[21], $NiO/Ni(OH)_2$[22,23], binary Ni-Co hydroxide[24], etc.[25–27] which introduce fast surface redox reactions. Previously, we reported the growth of high-quality graphene

and carbon nanotube (CNT) hybrid hierarchical nanostructures grown on high porosity nickel foam via one-step ambient pressure chemical vapor deposition (APCVD)[7]. This novel few-layer graphene and CNT hybrid foam (GM) is a 3D graphene foam conformally covered with densely packed CNT networks. High performance SCs with long cycle stability had been demonstrated. However, the specific capacitance and energy density are still relatively low compared to the performance of pseudocapacitive metal oxide nanostructures. Among all pseudocapacitive materials, RuO_2 appears to be the most promising material for SCs with the following advantages: i) simple and scalable synthesis, ii) high capacitance, and iii) rapid charging-discharging. In this article, we developed a novel 3D sub-5 nm hydrous RuO_2 nanoparticles anchored to graphene and CNT hybrid foam (RGM) nanocomposite system, which demonstrates superior gravimetric capacitance (502.78 F g^{-1}) and areal capacitance (1.11 F cm^{-2}). We integrated the 3D GM architecture[28] and sol-gel synthesized hydrous RuO_2 nanoparticles by a simple and scalable dip coating process, which yields a novel few-layer graphene foam architecture conformally covered with hybrid networks of RuO_2 nanoparticles and anchored CNTs. The porous GM foam not only provides a large surface area for the loading of RuO_2 nanoparticles but also facilitates electrolyte infiltration[29]. The hybrid RGM nanocomposite network demonstrates a hierarchical and porous structure which enables enough electrolyte access to the active materials (CNT-RuO_2 network layer). At the same time, the embedded CNTs in the CNT-RuO_2 network layer works as a conductive framework. Our innovative RGM architecture offers seamless connections at the graphene and CNT interface and enhances the interfacial integrity of major components (active materials and current collector) which improves the conductivity of the whole electrode compared with other reported hybrid RuO_2 systems[30–32]. Good electrolyte access, enhanced conductivity, and improved charge transport further lead to very high active material utilization, smaller internal resistance (ESR $\sim$ 1Ω), superior rate capability, and cycling stability[33]. In addition to a very high specific capacitance compared with other previously reported pseudocapacitive systems, symmetric ECs based on this innovative RGM hybrid foam architecture could be cycled reversibly in a operational voltage window of 1.5 V, which is much larger than the majority of aqueous electrolyte supercapacitors ($\sim$1.0 V)[19,33–38]. The high specific capacitance and extended operational voltage window lead to an impressive maximum energy density of 39.28 Wh kg^{-1} and power density of 128.01 kW kg^{-1}. In addition to the capacitance and energy density enhancement, the SC also shows an excellent cycling stability of 106% capacitance retention over 8100 cycles. The slight capacitance enhancement (6%) observed after 8100 cycles might be due to the electrochemical activation of the active material which has also been found in GM SCs as reported previously[7]. Lastly, our RGM nanocomposite sytem demonstres a binder-free technique for preparing high-energy SC electrodes[39,40].

Results

Figure 1a shows the microstructural illustration of the synthesis process of the sub-5 nm RuO_2 nanoparticle anchored graphene and CNT hybrid foam (RGM). The GM hybrid nanostructure is grown on a nickel foam backbone via a typical one-step ambient pressure CVD process by introducing a mixture gas of H_2 and C_2H_2/C_2H_4 at 750°C[41]. As indicated in our previous work, the few-layer graphene foam works as both a current collector and a buffer layer which facilitates the conduction of electrons from active materials to current collectors and enhances the electrochemical stability of nickel foam by insulating it from the electrolyte. In addition, the embedment of the CNTs within the graphene layer provides a good electronic and mechanical connection between the active material (CNT-RuO_2 network layer) and the current collector (few-layer graphene foam covered nickel), which improves the mechanical stability
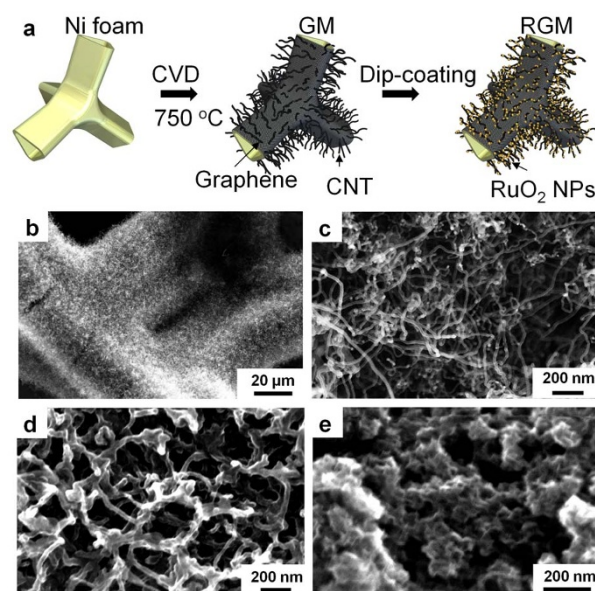
Figure 1 | Microstructure of RGM electrode. (a) Schematic illustration of the preparation process of RGM nanostructure foam. SEM images of (b–c) as-grown GM foam (d) Lightly loaded RGM, and (e) heavily loaded RGM.

and electronic conductivity of the system[41]. The porous GM foam serves as a perfect substrate for the loading of pseudocapacitive materials in the form of nanowires, nanoparticles and other nanostructures. Ruthenium oxide nanoparticles were synthesized according to literature with a modified sol-gel method as described in the experimental section[42]. The as-grown GM foams are mildly treated with UV-generated ozone for 60 seconds to enhance the surface wettability, and this process has been verified to be a nondestructive process[43]. X-ray diffraction (XRD) measurements were performed to confirm the phase and purity of the RuO_2 nanoparticles. The XRD pattern can be indexed as hydrous or amorphous RuO_2 nanoparticles which is in accordance with previously reported literature (Figure S1). Electron diffraction reaffirms that the crystals are hydrous or amorphous (Figure S2b). Different from other types of pseudo-capacitive materials such as V_2O_5, MnO_2, and NiO, etc., hydrous and amorphous forms of RuO_2 demonstrate better capacitive ability than anhydrous RuO_2. The higher energy density obtained by RuO_2 xH_2O is attributed to the mixed protonic-electronic conduction. The hydrous regions allow for facile proton permeation into the bulk material while the interconnected ruthenium oxide region accounts for electronic conduction[44,45].

The loading mass of carbonaceous material can be simply controlled with various growth conditions of the CVD process including time, catalyst amount, and carbon source concentration[41]. The loading amount of RuO_2 nanoparticles can be controlled by the surface morphology, wettability of GM foam, and the dispersion concentration of the nanoparticle suspension. The loading mass in this work is the total weight of few-layer graphene, CNTs and RuO_2 nanoparticles. This was obtained by measuring the weight change of the nickel foam before and after material loading.

Scanning electron microscopy (SEM) micrographs are shown to illustrate the structural and morphological properties of the as-grown GM foam, lightly loaded RGM nanocomposites, and heavily loaded RGM nanocomposites, respectively (Figure 1b–1e). Low magnification (Figure 1b) and high magnification (Figure 1c) are used to show the porous 3D GM foam with densely packed and randomly oriented CNTs, which possess a very large surface area (Langmuir and Brunauer-Emmett-Teller (BET) surface areas were found to be 743 and 497 m^2 g^{-1}, respectively[28]). Figure 1d and 1e

demonstrate the RGM foam with a different loading mass. High resolution (HR) TEM image demonstrates that the ultra-fine hydrous RuO_2 crystalline size is around 1–2 nm (Figure 2a and Figure S3). Hydrous RuO_2 nanoparticles tended to agglomerate to form larger particles after drying. Energy dispersive spectroscopy (EDS) microanalysis on a randomly selected area of a hydrous RuO_2 sample indicates that the sample consists of Ru, O, and traceable amount of Na from the reaction precursor (Figure 2b).

X-ray photoelectron spectroscopy (XPS) characterization was performed to confirm the hydrous nature of the as-synthesized RuO_2 nanoparticles. The survey XPS spectrum from our sample is provided in Figure S4. Although ruthenium is typically analyzed in XPS by following the strong singals from the 3d photoelectrons, here we used the 3p spectra instead in order to avoid interferences from the carbon substrates. The Ru $3p_{3/2}$ peak was deconvoluted into two components, which were identified with RuO_2 (462.2 eV)[46] and RuOH (464.1 eV). Those signals were found to exhibit an intensity ratio of 1 to 1.2 (Figure 3a). A similar ratio (1 : 1.3) is estimated from Ru-O-Ru, identified at 529.0 eV[47], and Ru-O-H, centered at 530.2 eV (Figure 3b). The XPS data in the C 1s region (Figure 3c) is quite complex, showing a total of seven components including peaks assigned to the Ru 3d photoelectrons, at 280.8 eV (Ru $3d_{5/2}$ of RuO_2[46], labeled A) and at 281.7 eV (a shake-up feature due to final state effects[48], labeled B). The peak at 283.3 eV, labeled C, was assigned to RuOH. The C 1s peak at 285.0 eV, from our support, was used for binding energy calibration; the rest of the components come from Ru $3d_{3/2}$ photoelectrons.

Two-electrode configuration symmetric SCs based on the RGM nanostructure foam electrodes were fabricated, which include two equal area RGM foam electrodes spaced apart by a porous separator. Cyclic voltammetry (CV) for RGM supercapacitors (SCs) was initially conducted at scanning rates between 10 mV sec^{-1} and 200 mV sec^{-1} in 2 M Li_2SO_4 aqueous electrolyte to estimate the capacitance and determine the useable voltage window. CV characteristics of the
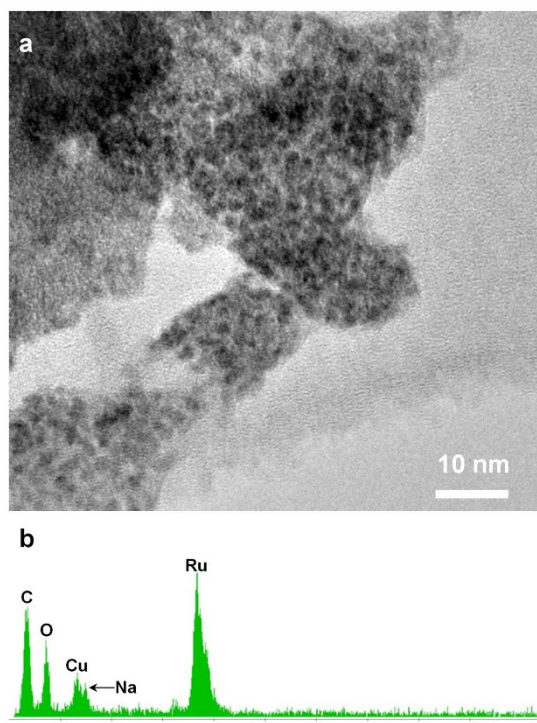
**Figure 2** | (a) HRTEM image of RuO_2 nanoparticles. (b) EDS spectrum of the RuO_2 nanoparticles showing the presence of the main components Ru, O along with minor amounts of sodium. Cu and C peak are background from the TEM support grid.
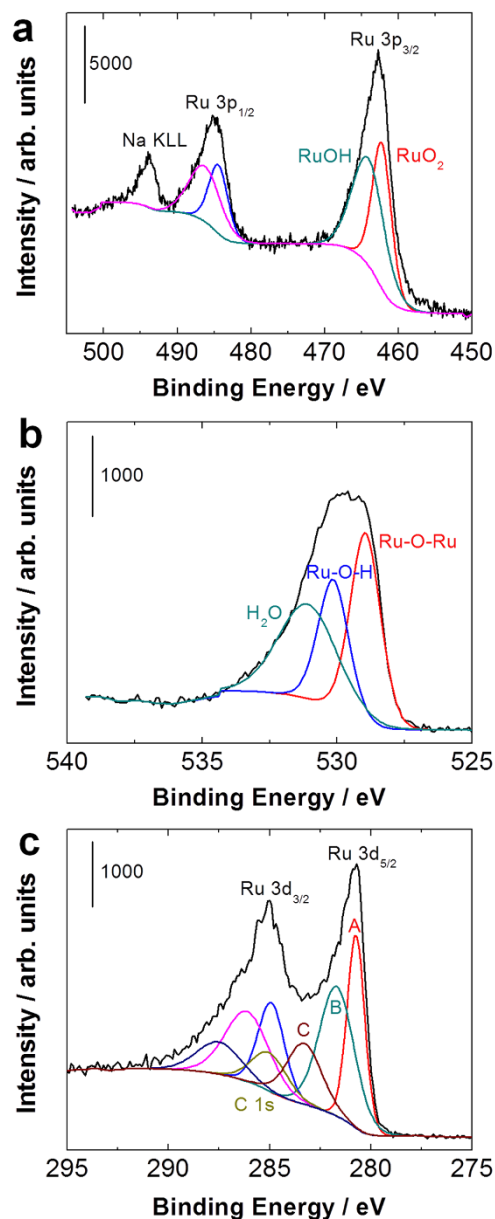
**Figure 3** | (a) Ru 3p, (b) O 1s, and (c) Ru 3d XPS spectra of hydrous RuO_2.

RGM supercapacitor with a range of various operational voltage windows at a scan rate of 50 mV s^{-1} are shown (Figure S5). With the increasing of potential limits from 1.0 to 1.8 Volts, more RuO_2 nanoparticles are involved in the surface-redox process. It is obvious that when the voltage window is increased beyond 1.8 V, an increasing amount of irreversible charge is observed which suggests the decomposition of aqueous electrolyte with hydrogen or oxygen evolution. It is impressive to see that no significant increase in anodic current is revealed at or below 1.5 V. These results suggest that the operation of this type of RGM supercapacitor with an exceptional operational voltage window of 1.5 V is feasible. This is comparable to certain assymmetric SC systems and much larger than the majority of aqueous electrolyte supercapacitors (~1.0 V) which are thermodynamically limited to a operational voltage window of 1.0 V due to the decomposition of water at 1.23 V[19,34–38]. We believe there are four possible reasons leading to the extended operational voltage window of the RGM SC system: (i) RuO_2 electrodes are capable of working in both negative and positive voltage windows which leads to a high operational voltage window for a packaged symmetric SC cell[49]. (ii) High hydrogen and oxygen evolution overpotentials of the RGM
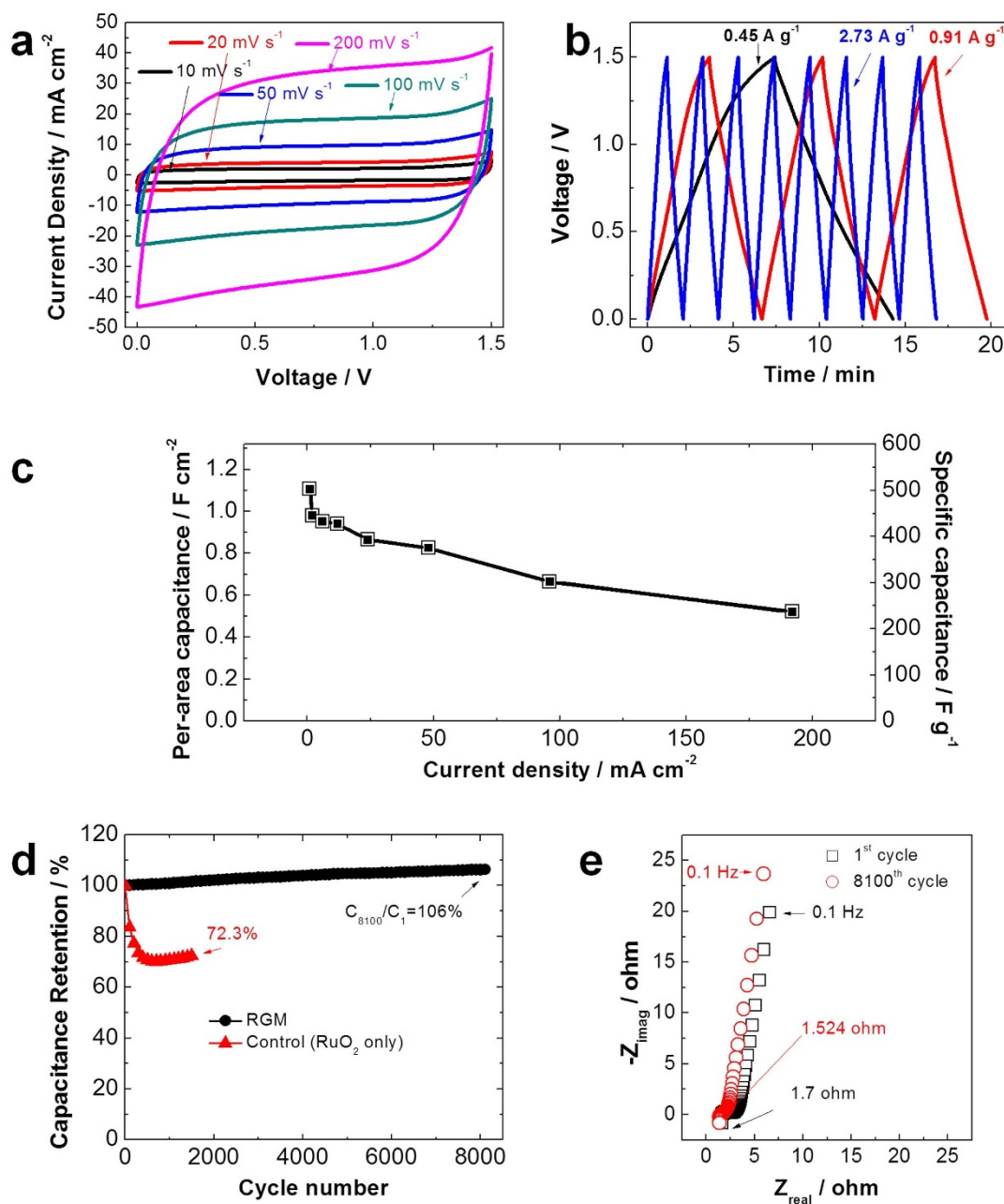
Figure 4 | Electrochemical performance of the supercapacitor based on RGM electrode. (a) Cyclic voltammetry measurements for RGM SC performed under different scan rates of 10, 20, 50, 100 and 200 mV s^{-1}. (b) Galvanostatic charge-discharge curves of a RGM SC at different current densities. (c) Specific capacitance and per-area capacitance of a RGM SC obtained from CC curves at different current densities. (d) Cyclic stability test of the RGM SC at the current density of 96 mA cm^{-2}. Data from control samples of pure RuO$_2$ nanoparticles are shown for comparison. (e) Plots of the potentiostatic electrochemical impedance spectroscopy (EIS) measurements conducted between 100 mHz and 1 MHz with an amplitude of 10 mV after 1st and 8100th cycle respectively.

electrodes in aqueous electrolyte due to the nanocrystalline nature of RuO$_2$[49]. (iii) Larger operational voltage window due to the usage of lithium sulfate aqueous solution as the electrolyte which has previously been confirmed[50]. (iv) Enhanced electrochemical stability of this innovative RGM foam architecture[51]. Figure 4a shows the near rectangular CV characteristics of the 3D RGM hybrid nanostructure foam with a potential window of 1.5 V under different scan rates. The nearly rectangular shape and the absence of oxidation and reduction peaks are observed for all scan rates suggesting that symmentric SCs based on RGM electrodes have near ideal capacitive behavior, small equivalent series resistance, high rate capability, and excellent electrochemical performance[52,53]. Moreover, the nearly

mirror-image shape of CV curves indicate exceptional reversibility and a very fast surface reaction[54]. Chronopotentiometry measurements were also conducted with a large operation voltage window of 1.5 V to further evaluate the electrochemical performance of the RGM foam supercapacitors. Charge-discharge (CC) characteristics with different current densities are shown in Figure 4b. The near linear and symmetric charge and discharge curves suggest an excellent capacitive performance with a rapid I-V response for our device. The calculated specific capacitances under different current densities below 200 mA cm^{-2} are shown in Figure 4c. The highest gravimetric capacitance of 502.78 F g^{-1} and areal capacitance of 1.11 F cm^{-2} were obtained at the same time under a current density of 1 mA
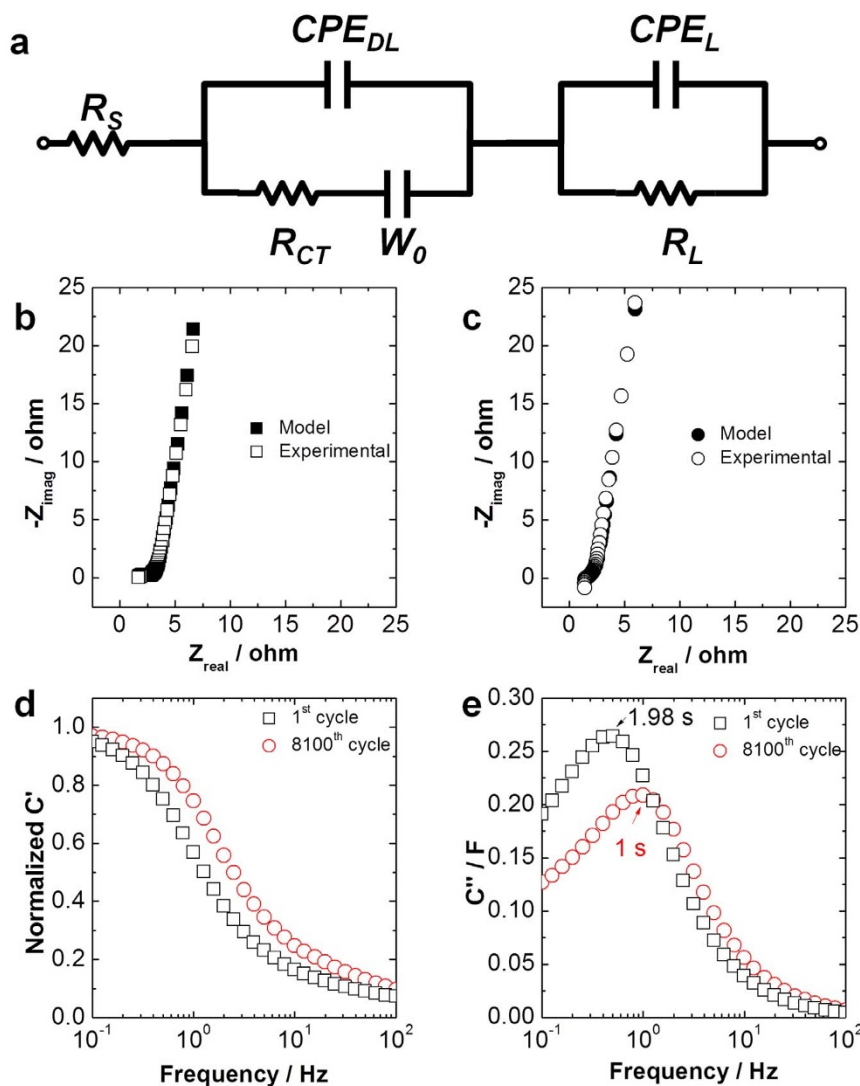
Figure 5 | Electrochemical Impedance Spectroscopy (EIS) study. (a) The equivalent circuit of Randle's model, where Rs is the equivalent series resistance (ESR), R_{CT} is the resistance of the electrode-electrolyte, R_L is the leakage resistance. CPE_{DL} is the constant phase element (CPE) of double layer, $W0$ is the Warburg element, CPE_L is the mass capacitance. Experimental and modeled Nyquist plots for complex impedance for RGM after (b) 1st cycle and (c) 8100th cycle. (d) Normalized real capacitance against frequency plot and (e) imaginary capacitance against frequency for RGM, and RGM after 8100 cycles.

cm^{-2}. Normally two mechanisms are involved in the storage of charges in the carbonaceous and pseudo-capacitive material hybrid electrodes[55].

Long cycling life is also one of the most critical factors for the application of supercapacitor electrodes. A sequence of charge-discharge cycles for our RGM nanostructure foam (Voltage window 1.5 V) and one control sample (Voltage window 1.0 V), which was based on RuO$_2$ nanoparticles on pristine nickel foam and GM foam under a current density of 96 mA cm^{-2} (Figure 4d). After 8100 cycles, superior capacitance retention (~106%) was maintained for the RGM nanostructure. The control sample was prepared via mixing hyrdous RuO$_2$ nanoparticles with 2% PVDF binder in NMP as the solvent. The slightly enhanced capacitance (6%) observed after 8000 cycles is perhaps due to reduced agglomeration of active material after cycling. The slight capacitance enhancement could also be due to the increased effective interfacial area between the RGM foam structure and the electrolyte with an increase in reaction time[35,56]. This self-strengthening effect also helps to stabilize the device during long term operation. We believe this binder-free design of oxide anchored nanocarbon hybrid supercapacitor architecture is promising for future energy storage applications.

Potentiostatic electrochemical impedance spectroscopy (EIS) measurements were performed to further characterize the performance of RGM SCs. Potentiostats are required to run impedance tests in a linear regime, so that test results remain consistent throughout[57]. The Nyquist plots obtained via EIS show that the RGM SC behaves approximately like an ideal supercapacitor in the low frequency region. This can be seen in both plots in Figure 4e (1st cycle and after 8100th cycle), where they show a near linear and vertical characteristic in this region[58,59]. Some deviation from absolute ideality is evident in a large but finite slope of the plot in this region. This can be a result of frequency dispersion due to a wider distribution of the pore size of the porous matrix[60].

The equivalent circuit used for fitting of the EIS plots in this work is shown in Figure 5a[61]. The EIS plots are fitted according to the model, and the as-fitted EIS plots are shown in Figure 5b–c. The fitted data for all circuit elements is shown in Table 1. Rs (also known as the solution resistance) is the equivalent series resistance (ESR), which generally describes the resistance of the electrolyte combined with the internal resistance of the electrode[62]. EIS plots after the 1st cycle and 8100th cycle were obtained to evaluate the internal resistance change during charge-discharge cycling (Figure 4e). Both

Table 1 | Fitted equivalent circuit elements of RGM before and after cycling

RGM	R_S	R_{CT}	CPE_{DL}	W_O	CPE_L
1st	1.7 Ω	1.02 Ω	Q_{DL} = 0.00095 n_{DL} = 0.635	W_{OR} = 2.5 W_{OC} = 0.42	Q_L = 0.16 n_L = 0.75
8100th	1.524 Ω	0.195 Ω	Q_{DL} = 0.011 n_{DL} = 0.65	W_{OR} = 3 W_{OC} = 0.5	Q_L = 0.13 n_L = 0.83

spectra possess a low ESR of approximately 1.5 Ω, which further demonstrates an exceptional electrochemical cycling stability of our hybrid nanostructure foam electrodes. This is evident as the nearly rectangular shape of the CV curves (Figure 4a) is maintained even in very high scan rates[63]. The decreased ESR (Table 1) from 1.7 ohm to 1.52 ohm after 8100 cycles may correspond to a reduction in internal resistance of the electrodes due to the electrochemical activation of active materials during cycling. R_{CT} (also known as charge transfer resistance) characterizes the rate of redox reactions at the electrode-electrolyte interface[64]. Low charge transfer resistance suggests fast ion transport within the SC[65]. We believe another factor contributing to the excellent cycling performance of the RGM nanostructure foam system is the embedment of CNTs within the graphene layer which helps to facilitate electronic conduction from the RuO_2 anchored CNT network layer to current collector (graphene coated nickel foam); this results in a reduced ESR. Additionally, the resultant relatively small charge transfer resistance should be associated with increased contact area at the electrode-electrolyte interface[66]. Thus, ion transfer and charge transfer is easily facilitated and reversibility is improved. CPE_{DL} is the constant phase element (CPE) representing double layer capacitance, which occurs at interfaces between solids and ionic solutions due to separation of ionic and/or electronic charges[62]. As shown in Table 1, the CPE_{DL} increases with cycling. This is due to reduced agglomeration of active material after cycling and activation of more material. Correspondingly, the available surface area increased as the supercapacitor was cycled repeatedly which is in accordance with the enhanced capacitance retention observed in Figure 4d. This hypothesis is also supported by the observed drop in R_{CT} after 8100 cycles. The double layer capacitance increased by ~1000% while charge transfer resistance decreased by ~80% after the RGM supercapacitor was cycled 8100 times. W_0 is the Warburg element, which represents the diffusion of ions into the porous electrode in the intermediate frequency region, and is a result of the frequency dependence of this diffusion. A possible reason for insensitivity to varying voltage scan rates is a short and equal diffusion path length of the ions in the electrolyte, as evidenced by a short Warburg region on the Nyquist plots[67]. R_L is the leakage resistance which is placed in parallel with CPE_L[68]. This is usually very high and can be ignored in the circuit. CPE_L denotes pseudocapacitance, which arises with voltage dependent Faradaic charge transfer processes. No significant change in pseudocapacitance is observed in RGM system before and after cycling[62].

Plots of normalized real capacitance vs. frequency and imaginary capacitance vs. frequency are shown in Figure 5d and 5e, respectively. The equations to derive C′(w) and C″(w) are given as supporting information. The device is treated as an ideal capacitor, and its complex capacitance is calculated from impedance data obtained via EIS using the formula Z = jwC[69,70]. In the C′(w) vs. frequency plot, it is observed that the RGM system after cycling retains its capacitive behavior for a higher frequency range, which is desirable (Figure 5d). The local maximum in the C″(w) vs. frequency plot shifts from 0.51 Hz to 1 Hz after cycling (Figure 4e). Therefore, the RGM system after 8100 cycles shows a 50% faster (from 1.98 s to 1 s) dielectric relaxation time characteristic compared to its pristine form[71]. This finding is in agreement with the decrease in ESR observed after cycling, because ESR is directly related to charge

and discharge time of the device (Table 1). Therefore, ion diffusion is further facilitated with increasing cycling numbers for the RGM system. All of these results support our claim of superior stability of the as-prepared RGM system.

In the real capacitance vs. frequency plot for the RGM system after 8100 cycles (Figure S7), we observe that the capacitance remains invariant for a larger frequency region. This is desirable and is indicative of ideal supercapacitive behavior[9]. Stability is more desirable than improvement in supercapacitor performance over a number of cycles. However, both stability and improvement are more desirable than deteriorating performance. The RGM system shows stability with minimal improvement with increasing cycling number. It does not show deterioration of capacity or of charge/discharge rate (dictated by dielectric relaxation time characteristic) after being cycled 8100 times.

The storage of charges in this RGM electrode is primarily contributed by the surface redox reaction of RuO_2 nanoparticles which has been verified by the CV characteristics of GM and RGM shown in Figure S6a. Besides enhanced cycling stability shown in Figure 4d, RGM also demonstrates higher capacitive behavior than the control sample based on RuO_2 nanoparticles due to improved electron-proton transport[72]. The EIS plots of GM, RGM, and a control sample made from RuO_2 nanoparticles only are shown to further characterize the excellent performance of our RGM system (Figure 6a, 6b). Although the anchoring of the sub-5 nm hydrous RuO_2 nanoparticles to the GM foam introduced a slight increase in ESR from 1.253 ohm to 1.7 ohm (Figure 6b), compared to the control samples based on nickel/RuO_2 electrode (ESR ~ 3.13 ohm) a much lower ESR is achieved with our RGM system(~46% decrease).

Discussion

To further evaluate the performance of the RGM foam for SC electrodes, we calculated the energy density (E) and power density (P) based on the chronopotentiometry measurements of our devices. The SC based on RGM hybrid electrodes exhibits a high energy density of 39.28 Wh kg⁻¹ at 0.356 kW kg⁻¹ which gradually reduces to 18.49 Wh kg⁻¹ at 128.01 kW kg⁻¹ (Table S1). Figure 6c shows a Ragone plot indicating energy density (E) versus power density (P) values of packaged RGM SC and GM SC[7] in detail, which suggests this innovative RGM SC is comparatively superior in performance compared to other types of RuO_2 or C-RuO_2 hybrid electrochemical capacitor systems[31,41,73,74]. The indicated E and P values are based on the mass of the active materials of the electrodes. Because the active material normally takes about ~1/3 of the total mass of the packaged commercial supercapacitors, the energy density or power density is frequently estimated to be the ~1/3 of the electrode material[75,76]. The maximum energy density of 13.09 Wh kg⁻¹ and the highest power density of 42.67 kW kg⁻¹ in aqueous electrolyte for packaged RGM SCs are still comparable to other types of electrochemical capacitor systems[1,31,41,73–75].These results suggests that our hybrid nanostructure foam is an exceptional candidate for future electrochemical capacitor and battery electrodes.

In summary, a novel 3D RGM foam has been demonstrated. This 3D RGM foam was prepared by ambient pressure chemical vapor deposition of a graphene and CNT foam structure and simple bath deposition of sub-5 nm hydrous RuO_2 nanoparticles. This method of preparing electrodes is a facile and scalable approach for high energy density supercapacitor applications. The two-step process successfully integrates the conformal coating of peseudocapacitive nanoparticles on the GM backbone to form an intertpenetrated network between CNTs and hydrous RuO_2 nanoparticles, which show an exceptional capacitive ability and high conductivity. The RGM electrode shows superior gravimetric and per-area capacitive performance (specific capacitance: 502.78 F g⁻¹, areal capacitance: 1.11 F cm⁻²) at the same time. The high specific/areal capacitance and extended operational voltage window of 1.5 V leads to an exceptionally high energy density
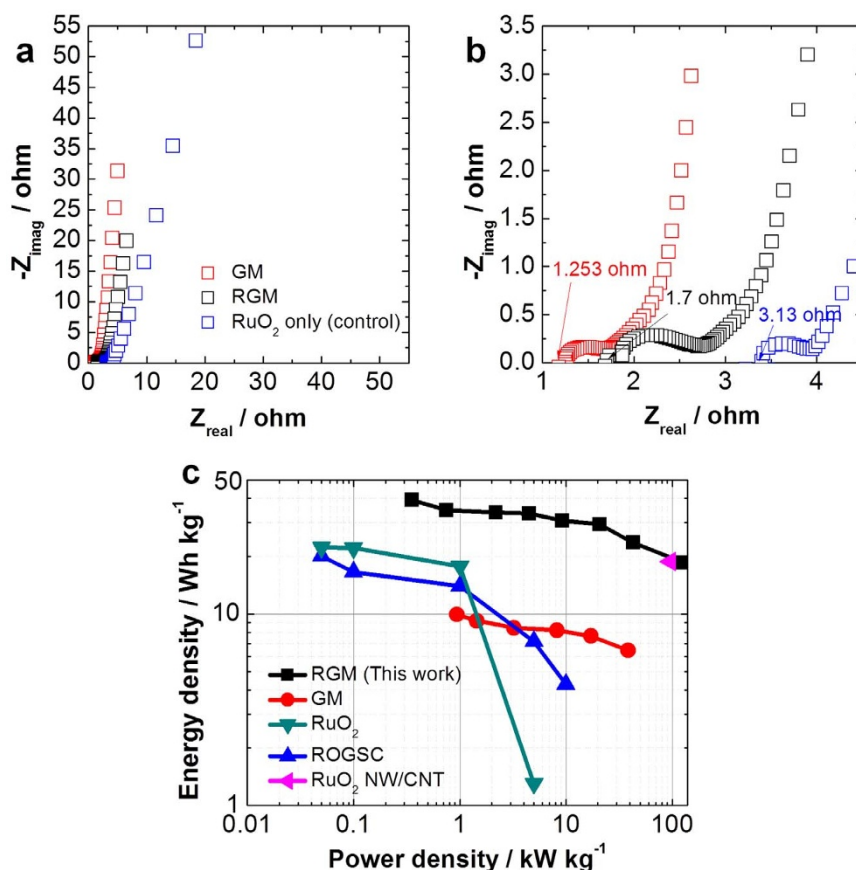
Figure 6 | (a) EIS plots and (b) high frequency region EIS plots of GM, RGM, a control sample (RuO$_2$ nanoparticles only), respectively. (c) Ragone plot related to energy densities and power densities of the packaged whole cell RGM SC, GM SC[7], RuO$_2$ nanoparticles SC[31], hydrous ruthenium oxide (RuO$_2$)/graphene sheets composite (GOGSC)[31], RuO2 nanowire/single walled carbon nanotube (SWNT) hybrid film[73].

of 39.28 Wh kg^{-1} and power density of 128.01 kW kg^{-1}. In addition to the capacitance and energy density enhancement, the RGM SC also shows an excellent cycling stability of ~106% capacitance retention over 8100 cycles. The electrochemical stability, excellent capacitive performance, and the easiness of the preparation method suggests this unique material system is promising for future high performance energy storage applications.

Methods

Materials synthesis. Graphene and CNTs foam was grown via a chemical vapor deposition (CVD) process by introducing a mixture of hydrocarbon (C$_2$H$_4$/C$_2$H$_2$) and hydrogen on 0.5 mm thick nickel foam[7]. A mild reactive ion etching (RIE) O$_2$-plasma is applied to nickel foam and 1–5 nm Fe catalysts are deposited by e-beam evaporation (Temescal, BJD-1800). The treated Ni foam is heated to 750°C, and hydrocarbon gas is introduced to trigger and continue the growth of graphene and CNTs synchronously on the nickel foam frame. Hydrous RuO$_2$ was synthesized according to literature with a modified sol-gel method[42]. In brief, a NaOH solution (1 M) was slowly injected into 100 ml RuCl$_3$ (0.1 M, Sigma Aldrich, USA) by a micro fluid system at a rate of 0.5 cm^3 min^{-1} to balance the PH to 7. *RuCl$_3$ + 3NaOH = Ru(OH)$_3$ + 3NaCl*. The mixed solution was stirred for another 12 hours, then centrifuged and washed with de-ionized (D. I.) water several times to remove the unwanted residual salts (NaCl). Next, the sample was vacuum dried at 120°C for 12 hours. The as-prepared hydrous RuO$_2$ nanoparticles were dispersed in D.I. water again to form a slurry like solution. The as-grown GM foam was treated with UV generated ozone for 60 seconds, and then it was dipped into the RuO$_2$ slurry to load the RuO$_2$ nanoparticles. After dip-coating, the hybrid RGM foam was dried and annealed at 150°C for 6 hours under vacuum. The as-synthesized RuO$_2$ nanoparticles were dispersed in D.I. water with an ultrasonic treatment to form a uniform gel-like suspension (concentration ~ 5 mg ml^{-1}). The resulting suspension was continuously stirred. The as-synthesized hydrous RuO$_2$ nanoparticles were incorporated into the GM foam structure by a simple dip coating process in the RuO$_2$ nanoparticle suspension. The sol-gel synthesized hydrous RuO$_2$ nanoparticles and GM foam exhibit intimate interfaces due to the abundance of hydrophilic groups on their surface, which yields an ultra-fine hydrous RuO$_2$ nanoparticles coated CNT network layer on graphene foam after vacuum drying.

Materials characterization. The surface morphology is investigated using optical microscopy, scanning electron microscopy (SEM; leo-supra, 1550) with an X-ray energy-dispersive spectroscopy (EDS), and transmission electron microscopy (TEM; Philips, CM300) with a LaB$_6$ cathode operated at 300 KV. The TEM samples were prepared by dispersing the as prepared RuO$_2$ nanoparticles in ethanol and then coating the dispersed nanoparticles onto carbon film coated TEM grid by simply dropping. X-ray photoelectron spectroscopy (XPS) characterization of the samples was carried out by using a Kratos AXIS Ultra DLD XPS system equipped with an Al Kα monochromated X-ray source and a 165-mm mean radius electron energy hemispherical analyzer. All binding energies were calibrated in reference to a value of 285.0 eV for the C 1s peak.

Fabrication and measurements of supercapacitor cells. A symmetrical packaged supercapacitor configuration was employed for the electrochemical measurements, where the two as-prepared RGM foams are assembled into a sandwich structure with a porous membrane (Celgard 3501), which functions as a separator. In this work, an aqueous electrolyte (2 M Li$_2$SO$_4$) is used. Cyclic voltammetry (CV), chronopotentiometry (charge-discharge (CD)), and electrochemical impedance spectroscopy (EIS) were conducted to evaluate the performance of the supercapacitors. Potentiostatic EIS measurements were performed between 0.1 Hz and 1 MHz with an amplitude of 10 mV. Specific capacitance C_s values are calculated from the charge-discharge curves via equation (1) $C_s = 2i/m(dV/dt)$. Where m is the mass of active material for one electrode, i is the discharge current and dV/dt is the slope of the discharge curve. The energy density (E) and power density (P) of the whole cell are calculated by using $E = 0.5C(\Delta V)^2$, and $P = E/t$, where t is the total time of discharge. C is the specific capacitance value of the supercapacitor cell which is equal to $0.25 C_s$, and ΔV is the potential range.

1. Simon, P. & Gogotsi, Y. Materials for electrochemical capacitors. *Nat. Mater.* **7**, 845–854 (2008).
2. Zhang, L. L. & Zhao, X. Carbon-based materials as supercapacitor electrodes. *Chem. Soc. Rev.* **38**, 2520–2531 (2009).
3. Wu, Z. S., Parvez, K., Feng, X. & Müllen, K. Graphene-based in-plane micro-supercapacitors with high energy and power densities. *Nat. Commun.* **4**, 1–8 (2013).

4. Pech, D. *et al*. Ultrahigh-power micrometre-sized supercapacitors based on onion-like carbon. *Nat. Nanotechnol.* **5**, 651–654 (2010).

5. Hu, L. *et al*. Highly conductive paper for energy-storage devices. *Proc. Natl. Acad. Sci.* **106**, 21490–21494 (2009).

6. Korenblit, Y. *et al*. High-rate electrochemical capacitors based on ordered mesoporous silicon carbide-derived carbon. *ACS Nano* **4**, 1337–1344 (2010).

7. Wang, W. *et al*. Three Dimentional Graphene-CNTs Foam Architectures for Electrochemical Capacitors. *ECS Trans.* **50**, 37–44 (2013).

8. Jung, H. Y. *et al*. Transparent, flexible supercapacitors from nano-engineered carbon films. *Sci. Rep.* **2**, 1–5 (2012).

9. Chmiola, J. *et al*. Monolithic carbide-derived carbon films for micro-supercapacitors. *Science* **328**, 480–483 (2010).

10. Kovalenko, I., Bucknall, D. G. & Yushin, G. Detonation Nanodiamond and Onion Like Carbon Embedded Polyaniline for Supercapacitors. *Adv. Funct. Mater.* **20**, 3979–3986 (2010).

11. Wang, W. *et al*. Hybrid Low Resistance Ultracapacitor Electrodes Based on 1-Pyrenebutyric Acid Functionalized Centimeter-Scale Graphene Sheets. *J. Nanosci. Nanotechnol.* **12**, 6913–6920 (2012).

12. Ghazinejad, M. *et al*. Synchronous chemical vapor deposition of large-area hybrid graphene–carbon nanotube architectures. *J. Mater. Res.* **28**, 958–968 (2013).

13. Wang, W., Guo, S., Ozkan, M. & Ozkan, C. S. Chrysanthemum like carbon nanofiber foam architectures for supercapacitors. *J. Mater. Res.* **28**, 912–917 (2013).

14. Guo, S., Wang, W., Ozkan, C. S. & Ozkan, M. Assembled graphene oxide and single-walled carbon nanotube ink for stable supercapacitors. *J. Mater. Res.* **28**, 918–926 (2013).

15. Chen, Z. *et al*. High-Performance Supercapacitors Based on Intertwined CNT/V2O5 Nanowire Nanocomposites. *Adv. Mater.* **23**, 791–795 (2011).

16. Perera, S. D. *et al*. Vanadium Oxide Nanowire–Carbon Nanotube Binder-Free Flexible Electrodes for Supercapacitors. *Adv. Energy Mater.* **1**, 936–945 (2011).

17. Hu, C.-C., Chang, K.-H., Lin, M.-C. & Wu, Y.-T. Design and tailoring of the nanotubular arrayed architecture of hydrous RuO2 for next generation supercapacitors. *Nano Lett.* **6**, 2690–2695 (2006).

18. Deng, L. *et al*. Graphene–MnO$_2$ and graphene asymmetrical electrochemical capacitor with a high energy density in aqueous electrolyte. *J. Power Sources* **196**, 10782–10787 (2011).

19. Dong, X.-C. *et al*. 3D Graphene–Cobalt Oxide Electrode for High-Performance Supercapacitor and Enzymeless Glucose Detection. *ACS Nano* **6**, 3206–3213, doi:10.1021/nn300097q (2012).

20. Meher, S. K. & Rao, G. R. Effect of microwave on the nanowire morphology, optical, magnetic, and pseudocapacitance behavior of Co3O4. *J. Phys. Chem. C* **115**, 25543–25556 (2011).

21. Bastakoti, B. P. *et al*. Mesoporous Carbon Incorporated with In2O3 Nanoparticles as High-Performance Supercapacitors. *Eur. J. Inorg. Chem.* **2013**, 1109–1112 (2013).

22. Nam, K.-W. & Kim, K.-B. A study of the preparation of NiO x electrode via electrochemical route for supercapacitor applications and their charge storage mechanism. *J. Electrochem. Soc.* **149**, A346–A354 (2002).

23. Wang, Y.-M. *et al*. Effect of electrodeposition temperature on the electrochemical performance of a Ni (OH) 2 electrode. *RSC Adv.* **2**, 1074–1082 (2012).

24. Bastakoti, B. P. *et al*. Hydrothermal Synthesis of Binary Ni–Co Hydroxides and Carbonate Hydroxides as Pseudosupercapacitors. *Eur. J. Inorg. Chem.* **2013**, 39–43 (2013).

25. Zhang, G. & Lou, X. W. D. Controlled Growth of NiCo2O4 Nanorods and Ultrathin Nanosheets on Carbon Nanofibers for High-performance Supercapacitors. *Sci. Rep.* **3**, 1–6 (2013).

26. Cheng, L. *et al*. Nanosized Li4Ti5O12 prepared by molten salt method as an electrode material for hybrid electrochemical supercapacitors. *J. Electrochem. Soc.* **153**, A1472–A1477 (2006).

27. Yuan, C. *et al*. Ultrathin Mesoporous NiCo2O4 Nanosheets Supported on Ni Foam as Advanced Electrodes for Supercapacitors. *Adv. Funct. Mater.* **22**, 4592–4597 (2012).

28. Lin, J. *et al*. Supercapacitors Based on Pillared Graphene Nanostructures. *J. Nanosci. Nanotechnol.* **12**, 1770–1775 (2012).

29. Soin, N. *et al*. Nanocrystalline ruthenium oxide dispersed Few Layered Graphene (FLG) nanoflakes as supercapacitor electrodes. *J. Mater. Chem.* **22**, 14944–14950, doi:10.1039/C2JM31226C (2012).

30. Liu, X., Huber, T. A., Kopac, M. C. & Pickup, P. G. Ru oxide/carbon nanotube composites for supercapacitors prepared by spontaneous reduction of Ru(VI) and Ru(VII). *Electrochim. Acta* **54**, 7141–7147, doi:http://dx.doi.org/10.1016/j.electacta.2009.07.044 (2009).

31. Wu, Z. S. *et al*. Anchoring Hydrous RuO2 on Graphene Sheets for High-Performance Electrochemical Capacitors. *Advanced Functional Materials* **20**, 3595–3602 (2010).

32. Huang, H. S. *et al*. Evaporation-Induced Coating of Hydrous Ruthenium Oxide on Mesoporous Silica Nanoparticles to Develop High-Performance Supercapacitors. *Small* **9**, 2520–2526 (2013).

33. He, Y. *et al*. Freestanding Three-Dimensional Graphene/MnO2 Composite Networks As Ultralight and Flexible Supercapacitor Electrodes. *ACS Nano* **7**, 174–182, doi:10.1021/nn304833s (2012).

34. Lang, X., Hirata, A., Fujita, T. & Chen, M. Nanoporous metal/oxide hybrid electrodes for electrochemical supercapacitors. *Nat. Nano.* **6**, 232–236, doi:http://

35. Fan, Z. *et al*. A three-dimensional carbon nanotube/graphene sandwich and its application as electrode in supercapacitors. *Adv. Mater.* **22**, 3723–3728, doi:10.1002/adma.201001029 (2010).

36. Yu, G. *et al*. Enhancing the Supercapacitor Performance of Graphene/MnO2 Nanostructured Electrodes by Conductive Wrapping. *Nano Lett.* **11**, 4438–4442, doi:10.1021/nl2026635 (2011).

37. Hou, Y., Cheng, Y., Hobson, T. & Liu, J. Design and Synthesis of Hierarchical MnO2 Nanospheres/Carbon Nanotubes/Conducting Polymer Ternary Composite for High Performance Electrochemical Electrodes. *Nano Lett.* **10**, 2727–2733, doi:10.1021/nl101723g (2010).

38. Wang, H., Gao, Q. & Jiang, L. Facile Approach to Prepare Nickel Cobaltite Nanowire Materials for Supercapacitors. *Small* **7**, 2454–2459, doi:10.1002/smll.201100534 (2011).

39. Lei, Z., Shi, F. & Lu, L. Incorporation of MnO2-Coated Carbon Nanotubes between Graphene Sheets as Supercapacitor Electrode. *ACS Appl. Mater. Interfaces* **4**, 1058–1064, doi:10.1021/am2016848 (2012).

40. Chen, Y. *et al*. One-pot synthesis of MnO2/graphene/carbon nanotube hybrid by chemical method. *Carbon* **49**, 4434–4442, doi:DOI 10.1016/j.carbon.2011.06.046 (2011).

41. Wang, W. *et al*. Three dimensional few layer graphene and carbon nanotube foam architectures for high fidelity supercapacitors. *Nano Energy* **2**, 294–303 (2013).

42. Wu, Z.-S. *et al*. Anchoring Hydrous RuO2 on Graphene Sheets for High-Performance Electrochemical Capacitors. *Adv. Funct. Mater.* **20**, 3595–3602, doi:10.1002/adfm.201001054 (2010).

43. Wang, H. Z. *et al*. Reversible transformation of hydrophobicity and hydrophilicity of aligned carbon nanotube arrays and buckypapers by dry processes. *Carbon* **48**, 868–875, doi:DOI 10.1016/j.carbon.2009.10.041 (2010).

44. Sugimoto. *et al*. Proton and Electron Conductivity in Hydrous Ruthenium Oxides Evaluated by Electrochemical Impedance Spectroscopy: The Origin of Large Capacitance. *J. Phys. Chem. B* **109**, 7330–7338, doi:10.1021/jp044252o (2005).

45. Fu, R., Ma, Z. & Zheng, J. P. Proton NMR and dynamic studies of hydrous ruthenium oxide. *J. Phys. Chem. B* **106**, 3592–3596 (2002).

46. Salomonsson, A. *et al*. Nanocrystalline ruthenium oxide and ruthenium in sensing applications–an experimental and theoretical study. *J. Nanopart. Res.* **8**, 899–910 (2006).

47. Hudec, B. *et al*. Impact of plasma treatment on electrical properties of TiO2/RuO2 based DRAM capacitor. *J. Phys. D: Appl. Phys.* **46**, 385304 (2013).

48. Cox, P. *et al*. The electronic structure of Bi$_{2-x}$ Gd$_x$ Ru$_2$ O$_7$ and RuO$_2$: A study by electron spectroscopy. *J. Solid State Chem.* **62**, 360–370 (1986).

49. Zhou, D.-D., Liu, H.-J., Wang, Y.-G., Wang, C.-X. & Xia, Y.-Y. Ordered mesoporous/microporous carbon sphere arrays derived from chlorination of mesoporous TiC/C composite and their application for supercapacitors. *J. Mater. Chem.* **22**, 1937–1943 (2012).

50. Fic, K., Lota, G., Meller, M. & Frackowiak, E. Novel insight into neutral medium as electrolyte for high-voltage supercapacitors. *Energy Env. Sci.* **5**, 5842–5850 (2012).

51. Wang, W. *et al*. Intertwined Nanocarbon and Manganese Oxide Hybrid Foam for High-Energy Supercapacitors. *Small* **9**, 3714–3721 (2013).

52. Stoller, M. D. & Ruoff, R. S. Best practice methods for determining an electrode material's performance for ultracapacitors. *Energy Env. Sci.* **3**, 1294–1301 (2010).

53. Xia, H. *et al*. A Symmetric RuO2/RuO2 Supercapacitor Operating at 1.6 V by Using a Neutral Aqueous Electrolyte. *Electrochem. Solid-State Lett.* **15**, A60–A63, doi:10.1149/2.023204esl (2012).

54. Wu, Z. S. *et al*. High-energy MnO2 nanowire/graphene and graphene asymmetric electrochemical capacitors. *ACS Nano* **4**, 5835–5842, doi:10.1021/nn101754k (2010).

55. Subramanian, V., Zhu, H. & Wei, B. Nanostructured MnO2: Hydrothermal synthesis and electrochemical properties as a supercapacitor electrode material. *J. Power Sources* **159**, 361–364, doi:http://dx.doi.org/10.1016/j.jpowsour.2006.04.012 (2006).

56. Wang, W. *et al*. Intertwined Nanocarbon and Manganese Oxide Hybrid Foam for High-Energy Supercapacitors. *Small* **9**, 3714–3721 (2013).

57. McKubre, M. C. H. & Macdonald, D. D. in *Impedance Spectroscopy* 129–204 (John Wiley & Sons, Inc., 2005).

58. Mishra, A. K. & Ramaprabhu, S. Functionalized graphene-based nanocomposites for supercapacitor application. *J. Phys. Chem. C* **115**, 14006–14013 (2011).

59. Buller, S., Karden, E., Kok, D. & De Doncker, R. in *Industry Applications Conference, 2001. Thirty-Sixth IAS Annual Meeting. Conference Record of the 2001 IEEE.* 2500–2504 (IEEE).

60. Song, H.-K., Hwang, H.-Y., Lee, K.-H. & Dao, L. H. The effect of pore size distribution on the frequency dispersion of porous electrodes. *Electrochim. Acta* **45**, 2241–2257 (2000).

61. Hastak, R. *et al*. All solid supercapacitor based on activated carbon and poly [2, 5-benzimidazole] for high temperature application. *Electrochim. Acta* **59**, 296–303 (2012).

62. Conway, B., Birss, V. & Wojtowicz, J. The role and utilization of pseudocapacitance for energy storage by supercapacitors. *J. Power Sources* **66**, 1–14 (1997).

63. Zhu, Y. *et al*. Carbon-Based Supercapacitors Produced by Activation of Graphene. *Science* **332**, 1537–1541, doi:10.1126/science.1200770 (2011).

64. Sluyters-Rehbach, M. Impedances of electrochemical systems: Terminology, nomenclature and representation-Part I: Cells with metal electrodes and liquid solutions. *Pure Appl. Chem.* **66**, 1831–1831 (1994).
65. Pan, L. *et al.* Hierarchical nanostructured conducting polymer hydrogel with high electrochemical activity. *Proc. Natl. Acad. Sci.* **109**, 9287–9292 (2012).
66. Choi, B. G. *et al.* 3D macroporous graphene frameworks for supercapacitors with high energy and power densities. *ACS Nano* **6**, 4020–4028 (2012).
67. Stoller, M. D., Park, S., Zhu, Y., An, J. & Ruoff, R. S. Graphene-based ultracapacitors. *Nano Lett.* **8**, 3498–3502 (2008).
68. Masarapu, C., Zeng, H. F., Hung, K. H. & Wei, B. Effect of temperature on the capacitance of carbon nanotube supercapacitors. *ACS nano* **3**, 2199–2206 (2009).
69. Choi, B. G., Hong, J., Hong, W. H., Hammond, P. T. & Park, H. Facilitated ion transport in all-solid-state flexible supercapacitors. *ACS nano* **5**, 7205–7213 (2011).
70. Taberna, P.-L., Portet, C. & Simon, P. Electrode surface treatment and electrochemical impedance spectroscopy study on carbon/carbon supercapacitors. *Appl. Phys. A* **82**, 639–646 (2006).
71. Chmiola, J., Yushin, G., Dash, R. & Gogotsi, Y. Effect of pore size and surface area of carbide derived carbons on specific capacitance. *J. Power Sources* **158**, 765–772 (2006).
72. Chen, L. *et al.* Toward the Theoretical Capacitance of RuO2 Reinforced by Highly Conductive Nanoporous Gold. *Adv. Energy Mater.* **3**, 851–856 (2013).
73. Chen, P. C., Chen, H. T., Qiu, J. & Zhou, C. W. Inkjet Printing of Single-Walled Carbon Nanotube/RuO2 Nanowire Supercapacitors on Cloth Fabrics and Flexible Substrates. *Nano Res.* **3**, 594–603, doi:DOI 10.1007/s12274-010-0020-x (2010).
74. Chen, Z. *et al.* High-Performance Supercapacitors Based on Intertwined CNT/V2O5 Nanowire Nanocomposites. *Adv. Mater.* **23**, 791–795, doi:10.1002/adma.201003658 (2011).
75. Gogotsi, Y. & Simon, P. True performance metrics in electrochemical energy storage. *Science* **334**, 917–918 (2011).
76. Zhang, L. *et al.* Porous 3D graphene-based bulk materials with exceptional high surface area and excellent conductivity for supercapacitors. *Sci. Rep.* **3**, 1–9 (2013).

Acknowledgments

Author contributions

W.W., S.G., M.O. and C.S.O. designed the experiments and wrote the main manuscript. W.W., S.G., Z.F. and J.Z. worked on materials synthesis, supercapacitor fabrication, galvanostatic charge-discharge measurements, cyclic stability tests, and electrochemical impedance spectroscopy (EIS) measurements. K.A. performed analysis for fitting equivalent circuit parameters. I.L. and F.Z. performed XPS analysis. C.S.O. managed the research team. All authors reviewed the manuscript.

Additional information

Supplementary information accompanies this paper at http://www.nature.com/scientificreports

Competing financial interests: The authors declare no competing financial interests.

How to cite this article: Wang, W. *et al.* Hydrous Ruthenium Oxide Nanoparticles Anchored to Graphene and Carbon Nanotube Hybrid Foam for Supercapacitors. *Sci. Rep.* **4**, 4452; DOI:10.1038/srep04452 (2014).